ChemComm

COMMUNICATION

View Article Online
View Journal

Cite this: DOI: 10.1039/c9cc03406d

Received 3rd May 2019,
Accepted 4th July 2019

DOI: 10.1039/c9cc03406d

rsc.li/chemcomm

Asynchronous reactions of "self-matrix" dual-crystals effectively accommodating volume expansion/shrinkage of electrode materials with enhanced sodium storage†

Youchen Hao,[ab] Xifei Li,[*abcd] Wen Liu,[ab] Hirbod Maleki Kheimeh Sari,[ab] Jian Qin[ab] and Yingying Li[c]

The large volume expansion of FeS_2 is successfully accommodated *via* a series of asynchronous redox reactions of dual-crystalline FeS_2. Consequently, a durable sodium storage performance with a reversible capacity of 567.7 mA h g^{-1} is obtained at 0.1 A g^{-1} after 50 cycles. This novel strategy can also be utilized in other types of electrodes having large volume change upon cycling.

As one of the most essential electrochemical parameters, specific capacity has been always used to measure the general properties of energy storage materials.[1,2] Generally, energy storage reactions are divided into insertion/desertion-, conversion- and alloy-type reactions,[3] among them the two latter ones with more electron transformation are considered as the most promising energy storage reactions regarding the high specific capacity. For instance, 1 mol silicon (Si) can attach with 4.4 mol e^- in lithium-ion batteries upon whole cycling, thereby leading to a striking theoretical specific capacity of 4200 mA h g^{-1}.[4] Similarly, phosphorus (P) and tin (Sn) can deliver an outstanding theoretical sodium storage capacity as high as 2596 mA h g^{-1} and 994 mA h g^{-1}, respectively.[5–8]

It is noteworthy that all of these multiple electron transition reactions easily cause a large volume expansion which may result in cracking, peeling and even dying out of active materials.[9] So far, enormous efforts have been devoted to deal with the volume expansion of these materials.[10–12] For example, a 1D silicon nanowire was synthesized to overcome this issue.[13] Benefiting from the good radial strain tolerance of the Si nanowire, an excellent lithium storage performance along with long cycling was obtained.[14,15] Liu *et al.*[6] synthesized red P@Ni-P (RP@Ni-P) with a controllable core–shell nanostructure as an anode material for sodium-ion batteries (SIBs) *via* a series of activation, electroless deposition and chemical de-alloying routes. The optimized RP@Ni-P composites delivered a superb capacity of 1256.2 mA h g^{-1} after 200 cycles at 0.1 C as well as remarkable rate capability and cycle-life, *i.e.*, a capacity of 409.1 mA h g^{-1} after cycling 2000 times at a high current density of 5 A g^{-1}. Moreover, an ultra-long lifespan with excellent performance (~10% capacity fading after 20000 cycles) and rate capability (170 mA h g^{-1} at 20 A g^{-1}) were obtained for pyrite FeS_2 with an insertion/desertion-type reaction by choosing a more appropriate electrolyte and adjusting the cut-off voltage to 0.8 V.[16] Although great progress has been made thus far in the electrode materials with large volume change upon cycling, more studies are still required to develop simple, low-cost and scalable methods to cope with this issue in a more practical manner.

Herein, we propose a novel strategy for accommodating the large volume variation, resulting from the transmission of multiple electrons. Taking FeS_2 as an example, the dual-crystalline material (pyrite and marcasite) obviously shows enhanced electrochemical capability and stability compared to the generally reported single one due to the dispersed internal stress stemming from the split redox peaks of the dual-crystal and the synergistic effect between the nanoscale mixed two phases. This work introduces the use of asynchronous reactions of dual-crystals to release the concentrated stress at redox peaks of single crystals.

To alleviate the large volume expansion and low conductivity of FeS_2,[17] carbon nanotubes (CNTs) were introduced as a flexible matrix. Various FeS_2 dual-crystal/CNT composites (denoted as bi-FeS_2-I, -II and -III, respectively) were synthesized *via* a hydrothermal method followed by a post gas-solid sulfurization process. Because of the relatively large surface area of multiwall CNTs (Fig. S1, ESI†), FeOOH with different ratios tends to grow on the surface of CNTs *via* the hydrothermal method (denoted as CNT@FeOOH-X, X = I, II and III) as depicted in SEM images in Fig. 1a, b and Fig. S2 (ESI†).

[a] Institute of Advanced Electrochemical Energy & School of Materials Science and Engineering, Xi'an University of Technology, Xi'an, Shaanxi 710048, China
[b] Shaanxi International Joint Research Centre of Surface Technology for Energy Storage Materials, Xi'an, Shaanxi 710048, China
[c] College of Physics and Materials Science, Tianjin Normal University, Tianjin 300387, P. R. China
[d] State Center for International Cooperation on Designer Low-carbon & Environmental Materials (CDLCEM), Zhengzhou University, 100 Kexue Avenue, Zhengzhou 450001, China. E-mail: xfli2011@hotmail.com

† Electronic supplementary information (ESI) available. See DOI: 10.1039/c9cc03406d

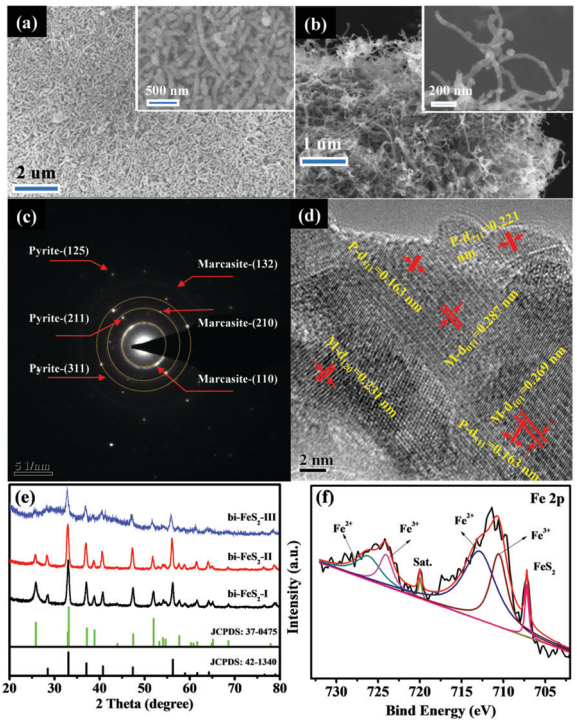

Fig. 1 High- (the insets) and low-magnification SEM images of (a) CNT@FeOOH-II and (b) bi-FeS_2-II. (c) SAED pattern and (d) HRTEM image of bi-FeS_2-II. (e) XRD patterns of bi-FeS_2-I, bi-FeS_2-II and bi-FeS_2-III. The high-resolution (f) Fe 2p XPS spectra of bi-FeS_2-II.

In the following sulfurization step, however, morphologies of the three samples were considerably changed with the growth of FeS_2 crystals at a high annealing temperature of 500 °C. In particular, the as-prepared bi-FeS_2-III displayed an apparent aggregation, while both bi-FeS_2-I and bi-FeS_2-II revealed a well dispersion of bi-FeS_2 in the CNT matrix (Fig. 1b and Fig. S2c, d, ESI†). By comparing the morphologies of the pure FeOOH and its sulfurized products in Fig. S3 with Fig. S2 (ESI†), it can be deduced that the introduction of flexible CNTs in bi-FeS_2 composites can not only enhance the electrochemical properties of the active materials through cycling, but also hamper the aggregation of FeS_2 during the sulfurization process.

The X-ray diffraction (XRD) pattern of the pure FeOOH is shown in Fig. S4a (ESI†), which corresponds to the tetragonal phase of FeOOH (JCPDS Card No. 75-1594). After the sulfurization step, all of the sulfurized samples present a mixed pyrite (JCPDS Card No. 42-1340) and marcasite (JCPDS Card No. 37-0475) phase, as depicted in Fig. 1e. According to the *K* value calculation method proposed by Gross and Martin,[18] the mass ratios of the two phases are almost 1 : 1 for all three samples (see Table S1, ESI†). As previously reported,[19,20] the formation of marcasite can be induced by the Ostwald ripening process, while the higher sulfurization temperature leads to the transition of marcasite to pyrite, thus causing various mass ratios of two phases in these dual-crystals. Meanwhile, the CNT contents in these composites were verified *via* thermogravimetric analysis (TGA) in an air atmosphere (Fig. S5, ESI†), and the contents of active materials in CNT@FeOOH-I, II, III and bi-FeS_2-I, II, III are calculated as 57.3%, 85.6%, 95.5% and 44.6%, 63.6%, 82.6%, respectively (see eqn (S1), ESI†). The surface species and element states of the as-prepared bi-FeS_2-II were further detected by X-ray photoelectron spectroscopy (XPS). The typical survey spectrum of FeS_2 is presented in Fig. S4b (ESI†) where the peaks of C 1s, S 2p and Fe 2p can be easily observed. In addition, the additional N peak at ~400 eV may have originated from the pyrolysis of thiourea in the sulfurizing procedure. In the high-resolution C 1s XPS spectrum (Fig. S4c, ESI†), the broad peak at around 285.5 eV can be assigned to the C–S bond, whereas the other peak at *ca.* 284.7 eV corresponds to the C=C bond.[21] Furthermore, the high-resolution Fe 2p XPS spectra are shown in Fig. 1f in which the dominant peaks at 712.7 eV for Fe $2p_{3/2}$ and 726.8 eV for Fe $2p_{1/2}$ are ascribed to Fe^{2+}, while the binding energies of 710.5 and 724.1 eV from the characteristic peaks of Fe $2p_{3/2}$ and Fe $2p_{1/2}$ correspond to the Fe^{3+} state which probably originates from FeOOH or surface oxidation of FeS_2.[22–24] Moreover, an obvious peak at 707 eV can be regarded as the characteristic peak of FeS_2. The S 2p spectrum of bi-FeS_2-II is deconvoluted into four peaks (Fig. S4d, ESI†). The typical S_n^{2-} peaks can be seen at 162.4 and 163.7 eV, whereas the peaks at 168.7 and 169.8 eV correspond to the oxidized groups of SO_4^{2-} and SO_3^{2-}.[25,26]

To further provide insight into the detailed microstructure feature of FeS_2 dual-crystals, transmission electron microscopy (TEM) was used to elucidate the as-obtained bi-FeS_2-II. As illustrated in Fig. S6 (ESI†), the refined FeS_2 particles are homogeneously distributed throughout the 3D CNT conductive networks. Notably, in the selected area electron diffraction (SAED) pattern depicted in Fig. 1c, two types of FeS_2 crystal, *i.e.*, (125), (211), and (311) for pyrite and (132), (210), and (110) for marcasite, exist which are in agreement with the XRD results. Furthermore, the high resolution TEM (HRTEM) image in Fig. 1d confirms the presence of both pyrite and marcasite phases which are randomly distributed. These nanoscale mixtures, which act as mutual restrictive matrices, may be helpful for the stabilization of the active materials.

Fig. 2a–c display the cyclic voltammetry (CV) curves of all dual-crystalline samples between 0.01 and 3 V at a scan rate of 0.1 mV s^{-1}. Evidently, all CV curves show similar redox peaks within the whole voltage window. According to a previous report,[27,28] the peak at ~1.1 V in the initial cathodic scan corresponds to the formation of solid–electrolyte interphase (SEI) films and the intercalation of Na^+ into FeS_2 dual-crystals. More strikingly, two adjacent reduction peaks at 0.4 and 0.25 V are simultaneously detected for the first time. Since there is a strong connection between the crystallographic structure and electrochemical performance,[29–31] these two reduction peaks may correspond to the further sodiation process of the two types of crystals. To date, few studies have focused on the application of marcasite FeS_2 in energy storage fields due to its instability under normal conditions.[20,32] Herein, pure pyrite FeS_2 was obtained by inducing phase transition of bi-FeS_2-II samples *via* annealing at a lower temperature of 400 °C for 2 h. As depicted in Fig. S7a and b (ESI†), these annealed products tend to aggregate because of the phase transformation and recrystallization of the precursors. Meanwhile, the crystallographic structure and phase purity of

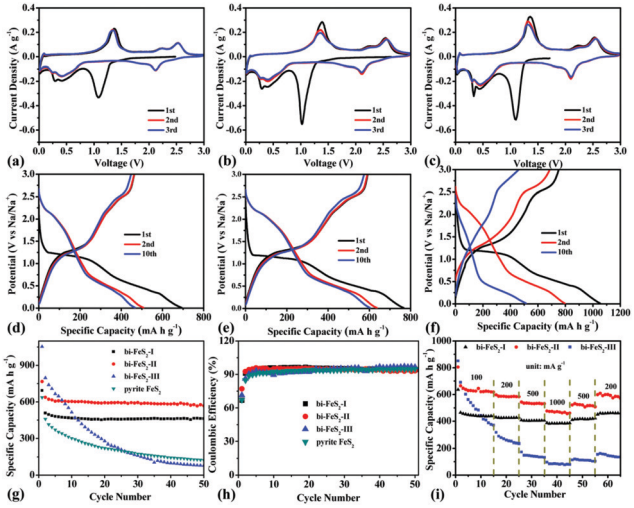

Fig. 2 CV curves and charge/discharge profiles of (a), (d) bi-FeS_2-I, (b), (e) bi-FeS_2-II and (c), (f) bi-FeS_2-III, respectively. (g) Cycling performance and (h) corresponding coulombic efficiency of the pyrite FeS_2 and bi-FeS_2-X (X = I, II and III). (i) Rate capability of bi-FeS_2-X (X = I, II and III) at various current densities from 0.1 to 1 A g^{-1}.

the as-prepared pyrite samples were examined and confirmed by XRD (Fig. S7c, ESI†). The characteristic CV curves of pyrite FeS_2 are given in Fig. S8a (ESI†), in which only a broad peak around 0.3 V can be found. Consequently, it is believed that the two pairs of redox peaks at 0.4/2.58 V and 0.25/2.25 V represent the partial redox peaks of pyrite and marcasite FeS_2, respectively. In addition, the two peaks at ~2.1/1.35 V portray the sodiation/desodiation potentials of $NaxFeS_2$ crystals.[33] Furthermore, the shrinking trend of the CV curves upon cycling demonstrates the intrinsic capacity fading of the pyrite FeS_2, while the overlapped curves of the initial several cycles show the excellent reversible electrochemical performance of the dual-crystalline FeS_2. Based on previous discussions on the sodium storage mechanism of Sn_4P_3,[34] these asynchronous reactions of the dual-crystal can efficiently avoid an excessive volume expansion because of the "self-matrix" effect between two phases, thereby prolonging the lifespan of electrodes. The evolution of these two types of electrodes (*i.e.*, single phase *vs.* dual-crystalline) is displayed in Scheme 1. The dual-crystalline phase is assumed to show a better cyclability mainly due to the synergistic effect of the two crystals.

To support the assumption mentioned above, the charge/discharge profiles of dual-crystalline FeS_2 and pyrite FeS_2 were tested at 100 mA g^{-1} between 0.01 and 3 V. As displayed in Fig. 2d–f, the bi-FeS_2-III hybrids exhibit an ultrahigh discharge capacity of 1053.2 mA h g^{-1} during the initial cycle, which is higher than those of bi-FeS_2-I (693.2 mA h g^{-1}) and bi-FeS_2-II (767 mA h g^{-1}) due to the high content of active materials. However, it is noticeable that only 460.9 mA h g^{-1} capacity of bi-FeS_2-III remains after 10 cycles, while both bi-FeS_2-I and bi-FeS_2-II show an excellent reversible capacity of 448.1 and 574.5 mA h g^{-1}, respectively. Apparently, apart from the initial irreversible capacity, both bi-FeS_2-I and bi-FeS_2-II exhibit a stable performance, while the fast capacity fading of bi-FeS_2-III may result from the irresistible pulverization upon cycling. Notably, although the pyrite FeS_2 is transformed from bi-FeS_2-II, its capacity fading according to Fig. S8b (ESI†) is even faster than the bi-FeS_2-III groups, *i.e.*, reversible capacity of almost 300 mA h g^{-1} after 10 cycles.

Furthermore, cyclic performance of the four electrodes and CNTs is exhibited in Fig. 2g and Fig. S9 (ESI†). The stability of all samples is well consistent with the observations of the charge/discharge profiles. After 50 cycles, bi-FeS_2-III can only deliver a reversible specific capacity of 79.1 mA h g^{-1} which is similar to the output of CNTs (around 70 mA h g^{-1}), while bi-FeS_2-I shows a high capacity retention of 91.4% compared to the second cycle (464.4 mA h g^{-1}). Indeed, the best performance by far is exhibited by bi-FeS_2-II which maintains a capacity of 567.7 mA h g^{-1} after 50 cycles. In contrast, the capacity fading trend of single phase FeS_2 is noticeably worse than the other samples in the initial several cycles, which is primarily induced by the over exhausted electrolyte and pulverization of active materials. Additionally, SEM images of the four electrodes before and after cycling are demonstrated in Fig. 3 and Fig. S10, S11 (ESI†). An evident erosion can be observed on the surface of the single phase FeS_2 electrode due to the large volume change, while all the dual-crystalline electrodes only reveal a slight dissolution after long cycling because of the escape of polysulfides.[22,35] Thus, the dual-crystalline materials are considered for the further investigation.

The coulombic efficiencies of all the composites are presented in Fig. 2h. The lowest coulombic efficiency (~92%)

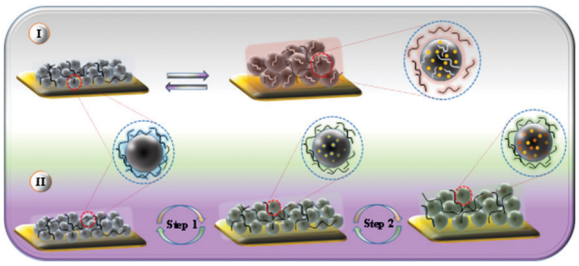

Scheme 1 The volume changes of (I) single phase FeS_2 and (II) dual-crystalline FeS_2 upon cycling.

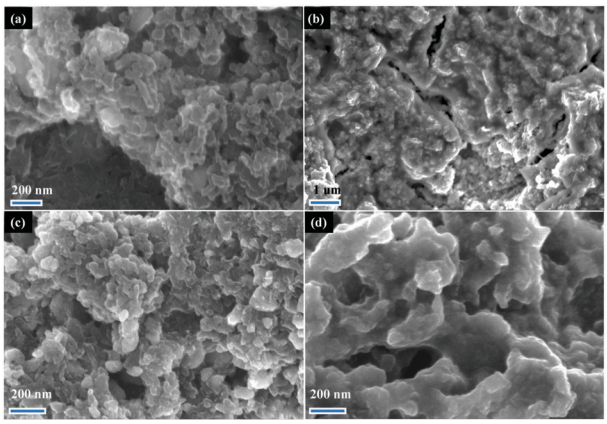

Fig. 3 SEM images of the pyrite FeS_2 and bi-FeS_2-II electrode surface (a), (c) before and (b), (d) after cycling, respectively.

belongs to bi-FeS_2-III which corresponds to its fast capacity fading during the initial 20 cycles, similar to the pyrite FeS_2 electrode. Meanwhile, the unexpected coulombic efficiency of bi-FeS_2-I and bi-FeS_2-II further demonstrates that the exposed active material may suffer from dissolution of polysulfides (see Fig. S12, ESI†), associating with the slight morphology change of cycled electrode mentioned above. Besides, the rate capability of bi-FeS_2-I, bi-FeS_2-II and bi-FeS_2-III was studied at various current densities, as shown in Fig. 2i. bi-FeS_2-III shows a poor rate performance with delivering a low specific capacity of only 85.2 mA h g^{-1} at a current density of 1 A g^{-1}, even when the current density returns back to 0.2 A g^{-1} again, it only remains 153.3 mA h g^{-1}. In contrast, both bi-FeS_2-II and bi-FeS_2-I deliver superb reversible capacities of 625.9, 583.6, 532.1, and 471.7 mA h g^{-1} and 441.5, 425.8, 404.2, and 382.4 mA h g^{-1}, respectively, at current densities of 0.1, 0.2, 0.5 and 1 A g^{-1}. This significant improvement of the electrochemical performance may be partly attributed to the optimized material mass ratio, the flexible CNT 3D conductive networks and the successive redox reactions of the dual-crystals upon cycling. This result corresponds well to the electrochemical impedance spectra (EIS) of these samples in Fig. S13 (ESI†), and higher conductivity is obtained with increasing CNT additive. Table S2 (ESI†) compares the reversible capacities of the single phase FeS_2 reported in previous studies with that of bi-FeS_2-II in this work. Notably, despite the broader voltage window in this work, the dual-crystal electrodes successfully exhibit superior cyclability and higher reversible capacity compared to the previously reported FeS_2. It is believed that the obtained results have the potential to be even further improved in the future. We believe that this result could be further enhanced with more efforts attempted by colleagues.

In this study, a novel dual-crystalline FeS_2 composite was synthesized which exhibited good sodium storage performance due to the asynchronous reactions of the mixed pyrite and marcasite phases, efficiently buffering the large volume expansion of FeS_2. As a result, the optimized bi-FeS_2-II delivered a reversible capacity of 567.7 mA h g^{-1} at 0.1 A g^{-1} after 50 cycles. Even at a high current density of 1 A g^{-1}, it still delivers an excellent specific capacity of 471.7 mA h g^{-1}. Indeed, the durable dual-crystalline FeS_2 shows a superior cyclability, remarkable sodium storage performance and alleviated volume expansion without sacrificing part of the conversion reactions. This study paves the way for further improvement in the capacity and life-span of dual-crystalline FeS_2 to ensure the practical application of this type of material in near future. Moreover, the applied strategy for controlling the volume expansion in this study may be an appropriate approach for other types of electrodes dealing with the contradiction between capacity and cyclability.

This work was supported by the National Key Research and Development Program of China (2018YFB0105900).

Conflicts of interest

The authors declare no competing financial interest.

Notes and references

1 J. B. Goodenough and Y. Kim, *Chem. Mater.*, 2010, **22**, 587–603.
2 V. Etacheri, R. Marom, R. Elazari, G. Salitra and D. Aurbach, *Energy Environ. Sci.*, 2011, **4**, 3243.
3 M. R. Palacin, *Chem. Soc. Rev.*, 2009, **38**, 2565–2575.
4 F. H. Du, Y. Ni, Y. Wang, D. Wang, Q. Ge, S. Chen and H. Y. Yang, *ACS Nano*, 2017, **11**, 8628–8635.
5 Y. Liu, A. Zhang, C. Shen, Q. Liu, X. Cao, Y. Ma, L. Chen, C. Lau, T. C. Chen, F. Wei and C. Zhou, *ACS Nano*, 2017, **11**, 5530–5537.
6 S. Liu, J. Feng, X. Bian, J. Liu, H. Xu and Y. An, *Energy Environ. Sci.*, 2017, **10**, 1222–1233.
7 P. Y. L. Ma, S. Wu, G. Zhu and Y. Shen, *J. Mater. Chem. A*, 2017, **5**, 16994–17000.
8 D. Cheng, J. Liu, X. Li, R. Hu, M. Zeng, L. Yang and M. Zhu, *J. Power Sources*, 2017, **350**, 1–8.
9 Y. Fang, L. Xiao, Z. Chen, X. Ai, Y. Cao and H. Yang, *Electrochem. Energy Rev.*, 2018, **1**, 292–323.
10 J.-T. Li, Z.-Y. Wu, Y.-Q. Lu, Y. Zhou, Q.-S. Huang, L. Huang and S.-G. Sun, *Adv. Energy Mater.*, 2017, **7**, 1701185.
11 W. Luo, X. Chen, Y. Xia, M. Chen, L. Wang, Q. Wang, W. Li and J. Yang, *Adv. Energy Mater.*, 2017, **7**, 1701083.
12 Q. Xia, W. Li, Z. Miao, S. Chou and H. Liu, *Nano Res.*, 2017, **10**, 4055–4081.
13 H. Ghassemi, M. Au, N. Chen, P. A. Heiden and R. S. Yassar, *ACS Nano*, 2011, **5**, 7805–7811.
14 C. K. Chan, H. Peng, G. Liu, K. McIlwrath, X. F. Zhang, R. A. Huggins and Y. Cui, *Nat. Nanotechnol.*, 2008, **3**, 31–35.
15 L.-F. Cui, Y. Yang, C.-M. Hsu and Y. Cui, *Nano Lett.*, 2009, **9**, 3370–3374.
16 Z. Hu, Z. Zhu, F. Cheng, K. Zhang, J. Wang, C. Chen and J. Chen, *Energy Environ. Sci.*, 2015, **8**, 1309–1316.
17 K. Zhang, M. Park, L. Zhou, G. H. Lee, J. Shin, Z. Hu, S. L. Chou, J. Chen and Y. M. Kang, *Angew. Chem., Int. Ed.*, 2016, **55**, 12822–12826.
18 S. T. Gross and D. E. Martin, *Ind. Eng. Chem. Res.*, 1944, **16**, 95–98.
19 D. Talapin, A. Rogach, E. Shevchenko, A. Kornowski, M. Haase and H. Weller, *J. Am. Chem. Soc.*, 2002, **124**, 5782.
20 T. Li, Z. Guo, X. Li, Z. Wu, K. Zhang, H. Liu, H. Sun, Y. Liu and H. Zhang, *RSC Adv.*, 2015, **5**, 98967–98970.
21 H. Shan, X. Li, Y. Cui, D. Xiong, B. Yan, D. Li, S. Lu and X. Sun, *Electrochim. Acta*, 2016, **205**, 188–197.
22 W. Chen, S. Qi, L. Guan, C. Liu, S. Cui, C. Shen and L. Mi, *J. Mater. Chem. A*, 2017, **5**, 5332–5341.
23 Y. Xiao, J.-Y. Hwang, I. Belharouak and Y.-K. Sun, *ACS Energy Lett.*, 2017, **2**, 364–372.
24 Y. X. Wang, J. Yang, S. L. Chou, H. K. Liu, W. X. Zhang, D. Zhao and S. X. Dou, *Nat. Commun.*, 2015, **6**, 8689.
25 E. Shangguan, L. Guo, F. Li, Q. Wang, J. Li, Q. Li, Z. Chang and X.-Z. Yuan, *J. Power Sources*, 2016, **327**, 187–195.
26 H. Geng, L. Zhu, W. Li, H. Liu, L. Quan, F. Xi and X. Su, *J. Power Sources*, 2015, **281**, 204–210.
27 Y. Zhu, L. Suo, T. Gao, X. Fan, F. Han and C. Wang, *Electrochem. Commun.*, 2015, **54**, 18–22.
28 Z. Liu, T. Lu, T. Song, X.-Y. Yu, X. Lou and U. Paik, *Energy Environ. Sci.*, 2017, **10**, 1576–1580.
29 T. Zhou, W. K. Pang, C. Zhang, J. Yang, Z. Chen, H. K. Liu and Z. Guo, *ACS Nano*, 2014, **8**, 8323–8333.
30 A. Robert Armstrong, Allan J. Paterson, Alastair D. Robertson and P. G. Bruce, *Chem. Mater.*, 2002, **14**, 710–719.
31 T. Wang, D. Su, D. Shanmukaraj, T. Rojo, M. Armand and G. Wang, *Electrochem. Energy Rev.*, 2018, **1**, 200–237.
32 H. Fan, H. Li, K. Huang, C. Fan, X. Zhang, X. Wu and J. Zhang, *ACS Appl. Mater. Interfaces*, 2017, **9**, 10708–10716.
33 A. Kitajou, J. Yamaguchi, S. Hara and S. Okada, *J. Power Sources*, 2014, **247**, 391–395.
34 J. Qian, Y. Xiong, Y. Cao, X. Ai and H. Yang, *Nano Lett.*, 2014, **14**, 1865–1869.
35 M. Walter, T. Zund and M. V. Kovalenko, *Nanoscale*, 2015, **7**, 9158–9163.

